First-principles modeling of x-ray Raman scattering spectra

E. de Clermont Gallerande, D. Cabaret, C. Brouder, M.-B. Attaiaa, L. Paulatto, K. Gilmore, Ch J Sahle, G. Radtke

Editors' Suggestion

First-principles modeling of x-ray Raman scattering spectra

E. de Clermont Gallerande,[1] D. Cabaret,[1] G. Lelong,[1] C. Brouder,[1] M.-B. Attaiaa,[1] L. Paulatto,[1] K. Gilmore,[2] Ch. J. Sahle,[2] and G. Radtke[1,*]

[1]*Sorbonne Université, Muséum National d'Histoire Naturelle, UMR CNRS 7590, IRD, Institut de Minéralogie, de Physique des Matériaux et de Cosmochimie, IMPMC, 75005 Paris, France*

[2]*European Synchrotron Radiation Facility, 38043 Grenoble, France*

(Received 28 August 2018; published 5 December 2018)

An efficient technique for calculating x-ray Raman scattering spectra at the K edge in the framework of a single-particle theory is presented. It is based on a recursive method to compute the dynamic structure factor as a continued fraction without requiring the explicit calculation of high-lying unoccupied electronic states. Multipole transitions are calculated to provide a full account of the q-dependence of K edges recorded in a series of lithium-bearing reference compounds, namely $LiBO_2$, Li_2CO_3, Li_2O, and LiF. The good agreement obtained between experimental and theoretical spectra validates our approach and provides a solid foundation for analyzing K edges beyond the dipole approximation.

DOI: 10.1103/PhysRevB.98.214104

I. INTRODUCTION

Since the pioneering experimental work of Suzuki and collaborators [1,2] during the late 1960s, x-ray Raman scattering (XRS) spectroscopy has become increasingly popular in condensed matter physics and chemistry, earth and material sciences as a tool for investigating the local atomic and electronic structure of solids [3–5], liquids [6–8], and gases [9,10]. Also known as nonresonant inelastic x-ray scattering (NRIXS), this technique indeed bears a lot of similarities with well established soft x-ray absorption spectroscopy (XAS) and electron energy loss spectroscopy (EELS), as it essentially probes the same electronic transitions under experimental conditions where the dipole approximation remains valid [11,12].

The use of hard x rays, however, makes this spectroscopy particularly well suited for studying low energy edges of bulk materials even under highly absorbing sample environments, opening up a wealth of possibilities for *in situ* experiments. This characteristic appears as a substantial advantage over XAS, where *in situ* measurements are largely hindered by the necessity of working in a high-vacuum environment and where the signal is essentially surface-sensitive, and over EELS, as this spectroscopy is often implemented in the transmission electron microscope with still rather limited *in situ* capabilities. A number of studies focused on pressure-induced structural modifications have therefore been carried out in XRS ranging from *in situ* monitoring of the π- to σ-bond conversion in layered compounds such as graphite [13] and hexagonal BN [14], variation of the unoccupied state orbital character in bulk silicon [15], to the detection of coordination changes in silicon [16–20], germanium [21], or boron [22,23] bearing crystalline and amorphous materials. Pressure has also been employed to explore the different phases of ice [24,25] and, combined with temperature, to probe the local structure of water under sub- and supercritical conditions. [26]

Another important advantage of XRS resides in its ability to control not only the energy, but also the momentum transferred to the photoelectron, both in magnitude and direction. Angular dependence studies of K edges have therefore been carried out with the purpose of determining the symmetry of unoccupied electronic states in hexagonal BN [5,27], MgB_2 [28], or in iridates [29] to measure crystal-field splittings. Dichroic signals have also been measured at shallow edges such as the cerium $N_{4,5}$ edge in unconventional heavy fermion superconductors $CeCu_2Si_2$ [30] and $CeCu_2Ge_2$ [31] for large magnitudes of the momentum transfer, allowing determination of the ground orbital states of these compounds.

The ability of XRS to transfer a large momentum and, thus, induce electric multipole transitions was indeed quickly recognized [32]. The most striking examples illustrating this aspect in XRS are undoubtedly the $N_{4,5}$ edges of lanthanides [33,34] and $O_{4,5}$ edges of actinides [35,36] where, when increasing the magnitude of the momentum transfer, giant dipole resonances progressively vanish while higher-order transitions appear at slightly lower energy losses, revealing a multiplet structure that eventually dominates the spectra. Nondipole transitions can also be probed at K edges of light elements [4,37–39] and consist predominantly of monopole or, usually to a much lesser extent, quadrupole transitions [40]. In this context, site specific angular-momentum projected local densities of states have been retrieved from sets of isotropic spectra recorded with different magnitudes of the momentum transfer [41], revealing the nature of the first unoccupied states in solids [25,42] and liquids [43].

Modeling therefore plays a very important role when interpreting the complex q-dependence of the XRS signal with the purpose of extracting useful information about the local atomic or electronic structure of a material. While atomic [44,45] or ligand-field [30,31] multiplet theories prove to be very successful in describing shallow edges characterized by

*guillaume.radtke@sorbonne-universite.fr

localized final states such as lanthanide $N_{4,5}$ or actinide $O_{4,5}$ edges, K edges are usually better described in the framework of single-particle theories. Different approaches have been developed for this purpose at different levels of approximation ranging from multiple-scattering theory within the *muffin-tin* approximation [4,46], full-potential density functional theory (DFT) calculations carried out in real space for clusters [40,47,48] or reciprocal space for periodic systems [49,50] to many-body perturbation theory by solving the Bethe-Salpeter equation (BSE) [51–54].

In this paper, we propose an efficient method for calculating XRS K edges based on DFT and implemented in the framework of the pseudopotentials and plane-wave method. In the same spirit as for XAS [55–57], the XRS dynamic structure factor is computed as a continued fraction through a recursive method, avoiding the explicit calculation of high-lying unoccupied states. In particular, multipole transitions are calculated to provide a full account of the q-dependence of K edges in a series of lithium-bearing reference compounds, namely $LiBO_2$, Li_2CO_3, Li_2O, and LiF.

The paper is organized as follows: In Sec. II, we give a brief account of the theory of XRS and describe its implementation in the framework of pseudopotentials. Section III provides all the necessary details related to the experiments and the calculations presented in this work. In Sec. IV, we present an extensive comparison between experimental and theoretical spectra, gathering all the K edges accessible in XRS on this set of compounds. Moreover, the different approximations employed to account for the presence of the core-hole in the final state and the associated technical issues are discussed in details. Our results on LiF are finally compared with those obtained using a more involved numerical approach based on solving the Bethe-Salpeter equation.

II. THEORY

A. XRS dynamic structure factor

In an inelastic x-ray scattering experiment, an incident photon, of wave vector, energy, and polarization direction ($\boldsymbol{k}_{\rm in}$, $\hbar\omega_{\rm in}$, $\hat{\varepsilon}_{\rm in}$), is scattered by an electron system. The scattered photon is similarly characterized by $\boldsymbol{k}_{\rm out}$, $\hbar\omega_{\rm out}$, and $\hat{\varepsilon}_{\rm out}$. A momentum $\boldsymbol{q}$ and an energy $\hbar\omega$, defined, respectively, by $\boldsymbol{q} = \boldsymbol{k}_{\rm in} - \boldsymbol{k}_{\rm out}$ and $\hbar\omega = \hbar\omega_{\rm in} - \hbar\omega_{\rm out}$, are thus transferred to the system [58]. The XRS double-differential scattering cross section can be written as [46]

$$\frac{d^2\sigma}{d\Omega\, d\omega}(\boldsymbol{q},\omega) = \frac{\omega_{\rm out}}{\omega_{\rm in}}\left(\frac{d\sigma}{d\Omega}\right)_{\rm Th} S(\boldsymbol{q},\omega), \tag{1}$$

where the Thomson scattering differential cross section reads

$$\left(\frac{d\sigma}{d\Omega}\right)_{\rm Th} = {r_0}^2\,(\hat{\varepsilon}_{\rm in}\cdot\hat{\varepsilon}^*_{\rm out})^2, \tag{2}$$

and the dynamic structure factor $S(\boldsymbol{q},\omega)$ is defined, in a single-particle framework, by

$$S(\boldsymbol{q},\omega) = \sum_f |\,\langle\psi_f|\,e^{i\boldsymbol{q}\cdot\boldsymbol{r}}\,|\psi_i\rangle\,|^2\delta(E_f - E_i - \hbar\omega). \tag{3}$$

In Eq. (2), r_0 is the classical radius of the electron. In Eq. (3), E_i and E_f are the energies of the initial core state $|\psi_i\rangle$ and the final state $|\psi_f\rangle$, respectively, and the transition operator can be expanded in terms of spherical harmonics as

$$e^{i\boldsymbol{q}\cdot\boldsymbol{r}} = 4\pi\sum_{\lambda=0}^{\infty}\sum_{\mu=-\lambda}^{\lambda} i^\lambda Y_\lambda^\mu(\hat{q})^* Y_\lambda^\mu(\hat{r})\, j_\lambda(qr), \tag{4}$$

where $j_\lambda(qr)$ is a spherical Bessel function. In Eq. (4), the zeroth ($\lambda = 0$), first ($\lambda = 1$), and second ($\lambda = 2$) -order terms lead to monopole, dipole, and quadrupole electronic transitions, respectively. In the low-q limit, dipole transitions are predominant. In such a case, it is worth noting that $S(\boldsymbol{q},\omega)$ becomes similar to the XAS cross section in the electric dipole approximation, the momentum transfer playing a role analogous with the polarization vector of the incident x-ray beam in XAS. A detailed comparison of the transition operator in both the XAS cross section and the XRS dynamic structure factor is given in the Appendix.

B. Implementation in a pseudopotential framework

In a pseudopotential approach, using the projector augmented wave (PAW) formalism [59], the dynamic structure factor can be written as

$$S(\boldsymbol{q},\omega) = \sum_f |\,\langle\widetilde{\psi}_f|\widetilde{\phi}_0\rangle\,|^2\,\delta(E_f - E_i - \hbar\omega), \tag{5}$$

where the pseudo final state $|\widetilde{\psi}_f\rangle$ is related to the all-electron final state $|\psi_f\rangle$, which is not directly computed, and

$$|\widetilde{\phi}_0\rangle = \sum_\nu |\widetilde{p}_{\mathbf{R}_0,\nu}\rangle\,\langle\phi_{\mathbf{R}_0,\nu}|\,e^{i\boldsymbol{q}\cdot\boldsymbol{r}}\,|\psi_i\rangle\,. \tag{6}$$

In Eq. (6), $|\phi_{\mathbf{R}_0,\nu}\rangle$ is an all-electron atomic partial wave centered on the absorbing atom site $\mathbf{R}_0$, defined in the Schrödinger representation as

$$\langle\boldsymbol{r}|\phi_{\mathbf{R}_0,\nu}\rangle = R_{p\ell\sigma}(r)Y_\ell^m(\hat{r})\chi_\sigma^s(s_z), \tag{7}$$

where $\boldsymbol{r} = r\hat{r}$, $R_{p\ell\sigma}$, Y_ℓ^m, and χ_σ^s are the radial, angular (complex spherical harmonics), and spin parts of $\phi_{\mathbf{R}_0,\nu}$, respectively. The $|\phi_{\mathbf{R}_0,\nu}\rangle$ all-electron partial wave coincides with the $|\widetilde{\phi}_{\mathbf{R}_0,\nu}\rangle$ corresponding pseudoatomic partial wave outside a spherical core region $\Omega_{\mathbf{R}_0}$. The $|\widetilde{p}_{\mathbf{R}_0,\nu}\rangle$ projector function, equal to zero outside $\Omega_{\mathbf{R}}$, satisfies the conditions $\langle\widetilde{p}_{\mathbf{R}',\nu'}|\widetilde{\phi}_{\mathbf{R}_0,\nu}\rangle = \delta_{\mathbf{R}',\mathbf{R}_0}\delta_{\nu'\nu}$. The compound index ν stands for quantum numbers (ℓ, m, σ) and an additional p number, used if there is more than one projector per angular momentum channel.

A general expression of $|\widetilde{\phi}_0\rangle$ valid for any edge requires the specification of a set of quantum numbers (n_i, ℓ_i, j, m_j) to describe the initial state $|\psi_i\rangle$, which accounts for the effect of spin-orbit coupling when $\ell_i \neq 0$. Using Eq. (4), and consistent with the notations of Ref. [57], it reads

$$\begin{aligned}|\widetilde{\phi}_0{}^{n_i,\ell_i,j,m_j}\rangle = 4\pi\sum_{\lambda=0}^{\infty}\sum_{\mu=-\lambda}^{\lambda} i^\lambda(-1)^\mu Y_\lambda^{-\mu}(\hat{q})\\ \times\sum_{\sigma=-1/2}^{1/2}(\ell_i\, m_j{-}\sigma\; s\;\sigma|j\; m_j)\\ \times\sum_{p,\ell}\mathcal{J}^\lambda_{p\ell,n_i\ell_i,\sigma}\sum_{m=-\ell}^{\ell}\mathcal{G}^{\ell,m}_{\lambda,\mu,\ell_i,m_j-\sigma}|\widetilde{p}_{\mathbf{R}_0,p,\ell,m,\sigma}\rangle.\end{aligned} \tag{8}$$

In Eq. (8), $(\ell_1 m_1 \ell_2 m_2 | \ell_3 m_3)$ is a Clebsch-Gordan coefficient, $\mathcal{G}$ is a Gaunt coefficient, and $\mathcal{J}^{\lambda}_{p\ell,n_i\ell_i,\sigma}$ is the radial integral defined by

$$\mathcal{J}^{\lambda}_{p\ell,n_i\ell_i,\sigma} = \int R_{p\ell\sigma}(r) R_{n_i\ell_i\sigma}(r) j_\lambda(qr) r^2 dr. \tag{9}$$

For an initial s state (K edges, L_1 edges, etc.), the monopole, dipole, and quadrupole terms of $|\widetilde{\phi}_0{}^{n_i,0,\frac{1}{2},\sigma}\rangle$ read, respectively,

$$|\widetilde{\phi}_0\rangle_{\text{mono}} = \sum_{p,\sigma} \mathcal{J}^{\lambda=0}_{p0,n_i0,\sigma} |\widetilde{p}_{\mathbf{R}_0,p,0,0,\sigma}\rangle , \tag{10}$$

$$|\widetilde{\phi}_0\rangle_{\text{dip}} = i\sqrt{3} \sum_{p,\sigma} \mathcal{J}^{\lambda=1}_{p1,n_i0,\sigma} \left(\frac{\hat{q}_x + i\hat{q}_y}{\sqrt{2}} |\widetilde{p}_{\mathbf{R}_0,p,1,-1,\sigma}\rangle + \hat{q}_z |\widetilde{p}_{\mathbf{R}_0,p,1,0,\sigma}\rangle + \frac{-\hat{q}_x + i\hat{q}_y}{\sqrt{2}} |\widetilde{p}_{\mathbf{R}_0,p,1,1,\sigma}\rangle \right), \tag{11}$$

$$\begin{aligned} |\widetilde{\phi}_0\rangle_{\text{quad}} = -\sqrt{\frac{15}{2}} \sum_{p,\sigma} \mathcal{J}^{\lambda=2}_{p2,n_i0,\sigma} \Bigg(& \frac{(\hat{q}_x - i\hat{q}_y)^2}{2} |\widetilde{p}_{\mathbf{R}_0,p,2,2,\sigma}\rangle \\ & + (-\hat{q}_x + i\hat{q}_y)\hat{q}_z |\widetilde{p}_{\mathbf{R}_0,p,2,1,\sigma}\rangle \\ & + \frac{3\hat{q}_z{}^2 - 1}{\sqrt{6}} |\widetilde{p}_{\mathbf{R}_0,p,2,0,\sigma}\rangle \\ & + (\hat{q}_x + i\hat{q}_y)\hat{q}_z |\widetilde{p}_{\mathbf{R}_0,p,2,-1,\sigma}\rangle \\ & + \frac{(\hat{q}_x + i\hat{q}_y)^2}{2} |\widetilde{p}_{\mathbf{R}_0,p,2,-2,\sigma}\rangle \Bigg), \end{aligned} \tag{12}$$

where $(\hat{q}_x, \hat{q}_y, \hat{q}_z)$ are the Cartesian coordinates of $\hat{q}$, the unit vector describing the orientation of $\boldsymbol{q}$ ($\boldsymbol{q} = q\hat{q}$).

For each monopole, dipole, or quadrupole transition, the dynamic structure factor [Eq. (5)] is calculated as a continued fraction, whose coefficients are obtained by building a Lanczos basis [60] for a fixed value of the norm of q. We thus neglect its energy dependence over the range employed to calculate the spectra, usually of a few tens of eV. Note that the relative variation $\Delta q/q$ is maximized for small scattering angles and small energy losses, i.e., typically for K edges of low-Z elements studied in this work. However, under the experimental conditions described in this paper, $\Delta q/q$ evaluated over an energy range of 50 eV is lower than 1%, justifying the above-mentioned approximation.

The dynamic structure factor depends on both the norm q and the orientation $\hat{q}$ of the momentum transfer $\boldsymbol{q}$. In the case of a powder sample, for a given value of q, the XRS spectrum can be calculated as a sum of isotropic λ-dependent contributions, since the cross-terms [i.e., terms between two different transition channels in the squared matrix element of Eq. (3)] cancel. By definition, the monopole ($\lambda = 0$) contribution is isotropic. Indeed, as shown in Eq. (10), $|\widetilde{\phi}_0\rangle_{\text{mono}}$ does not depend on $\hat{q}$. As is explicitly visible in Eqs. (11) and (12), the dipole ($\lambda = 1$) and quadrupole ($\lambda = 2$) contributions both depend on $\hat{q}$. The calculation of $S^{\text{iso}}_{\text{dip}}(q,\omega)$ and $S^{\text{iso}}_{\text{quad}}(q,\omega)$ requires the consideration of at most three and five distinct $\hat{q}$ orientations, respectively. However, these numbers can be reduced depending on the symmetries of the crystal point group.

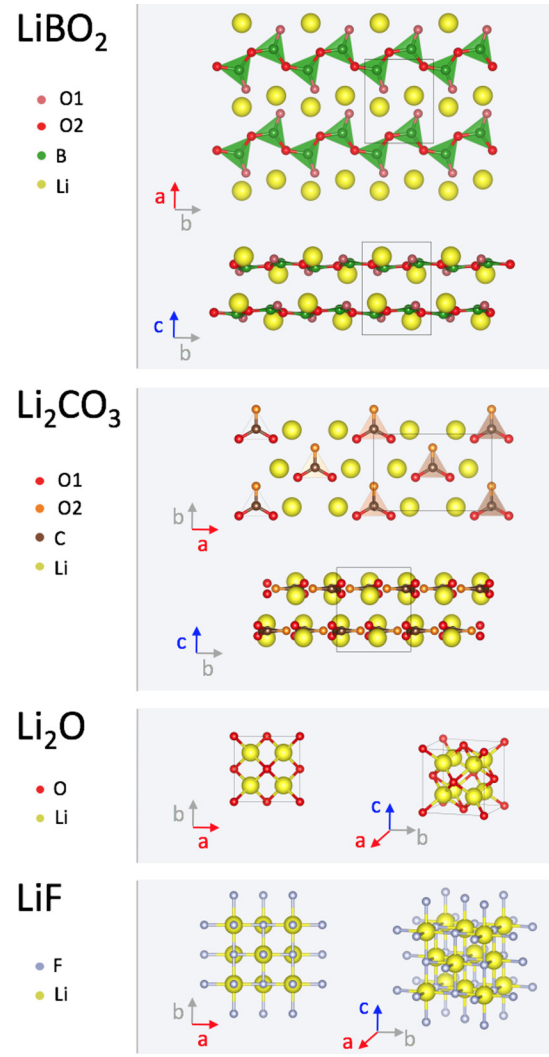

FIG. 1. Crystal structures of $LiBO_2$, Li_2CO_3, Li_2O, and LiF.

III. TECHNICAL DETAILS

A. Samples

This study was carried out on powder samples of lithium metaborate ($LiBO_2$), lithium carbonate (Li_2CO_3), lithium oxide (Li_2O), and lithium fluoride (LiF). Li_2CO_3 (99.99%), Li_2O (97%), and LiF (99.99%) were purchased at Alfa Aesar, Aldrich, and Sigma-Aldrich, respectively. $LiBO_2$ was synthesized from Li_2CO_3 and H_3BO_3 following a method described previously [65,66]. The powder samples were pressed into cylindrical powder pellets of 13 mm diameter and approximately 3 mm thickness.

The crystallographic structure of these four lithium compounds is displayed in Fig. 1. $LiBO_2$ has a monoclinic structure composed of infinite chains of BO_3 units parallel to [010] with two bridging oxygens and one nonbridging oxygen. Li_2CO_3 has a monoclinic structure with isolated triangular CO_3 units with one double C=O bond. In $LiBO_2$ and Li_2CO_3, Li atoms occupy distorted tetrahedral sites. Li_2O has a cubic structure with Li occupying all the tetrahedral interstitial sites of the cubic close packing of oxygens. Finally, LiF has a rocksalt cubic structure with both Li and F in octahedral sites.

TABLE I. Structure and supercells used for $LiBO_2$, Li_2CO_3, Li_2O, and LiF. Rhombohedral (rh) supercells were used in the case of face-centered-cubic lattices.

Compound	System	Space group	Lattice parameters	Inequivalent sites	Supercell	Shortest distance between excited atoms	Reference
$LiBO_2$	monoclinic	$P2_1/c$	$a = 5.838$ Å $b = 4.348$ Å $c = 6.449$ Å $\beta = 115.12°$	two sites of O	$2 \times 2 \times 2$ (128 atoms)	8.696 Å	Ref. [61]
Li_2CO_3	monoclinic	$C2/c$	$a = 8.390$ Å $b = 5.000$ Å $c = 6.210$ Å $\beta = 114.5°$	two sites of O	$1 \times 2 \times 2$ (96 atoms)	8.390 Å	Ref. [62]
Li_2O	cubic	$Fm\bar{3}m$	$a = 4.619$ Å		rh $3 \times 3 \times 3$ (81 atoms)	9.798 Å	Ref. [63]
LiF	cubic	$Fm\bar{3}m$	$a = 4.028$ Å		rh $3 \times 3 \times 3$ (54 atoms)	8.545 Å	Ref. [64]

B. Experiments

The K edges of all the elements constitutive of $LiBO_2$, Li_2CO_3, Li_2O, and LiF were recorded using x-ray Raman scattering spectroscopy. All experimental spectra were collected at the inelastic scattering beamline ID20 of the European Synchrotron Radiation Facility (ESRF), Grenoble, France.

The incident x rays were monochromatized using a combination of a high heat-load Si(111) monochromator and a Si(311) post monochromator and focused to a spot size of approximately 50×50 μm^2 at the sample position using a Kirkpatrick-Baez mirror assembly. XRS spectra of Li_2CO_3, Li_2O, and LiF were taken using the large-solid-angle x-ray Raman scattering spectrometer [67] employing 24 Si(660) analyzer crystals for momentum transfers of 4.5 ± 0.2 $Å^{-1}$ (low q) and 8.5 ± 0.1 $Å^{-1}$ (high q) and an overall energy resolution of 0.7 eV. The $LiBO_2$ data were recorded using the high-resolution spectrometer employing 5 Si(555) analyzer crystals in two different runs for momentum transfers of 2.4 ± 0.1 $Å^{-1}$ (low q) and 10.2 ± 0.1 $Å^{-1}$ (high q), respectively. The overall energy resolution was 0.6 eV for this second data set.

All experimental data were analyzed using the XRSTOOLS software package [68]. The integrated intensity of each spectra was normalized over a 40 eV energy range.

C. Calculations

1. Computational details

All the theoretical spectra were obtained using the XSPECTRA module in which we implemented the calculation of the XRS dynamic structure factor [see Eq. (5)] as a continued fraction, following the scheme adopted for x-ray absorption calculations [55,56]. XSPECTRA is a part of the QUANTUM ESPRESSO [69] suite of codes, which is based on DFT, uses a plane-wave basis set, pseudopotentials, and periodic boundary conditions. This reciprocal space approach implies the use of supercells to isolate the absorbing atom. The supercell has to be large enough to minimize the interaction between the absorbing atom and its periodically repeated images.

Two methods were employed to preserve charge neutrality of the supercell in the presence of a core hole for the absorbing atom: (i) the full-core-hole (FCH) approach, in which the excited electron is modeled as a uniform background charge within the supercell; and (ii) the excited-core-hole (XCH) approach [70], in which the excited electron is put in the lowest available unoccupied state so as to contribute to the local screening of the core hole. The XCH approach was used at the Li, B, and C K edges, while the FCH approach was preferred at the O and F K edges. Alternatively, the half-core-hole (HCH) approach was tested at the Li K edge. The HCH approximation consists in removing half an electron from the core state, thereby simulating a transition state in the x-ray excitation process. The choice of a given approach is discussed in Sec. IV C.

Ultrasoft pseudopotentials [71] were generated using the PSLIBRARY [72], in the Rappe, Rabe, Kaxiras, and Joannopoulos formalism [73], and within the generalized gradient approximation of Perdew, Burke, and Ernzerhof [74]. Each pseudopotential includes two s and p projectors, while a single d projector was added for lithium and fluorine to evaluate the quadrupole contributions in LiF. The pseudopotential of the absorbing atom was obtained by removing one $1s$ core electron (half an electron only in the HCH approximation) from its electronic configuration and by adjusting the ionic radii to slightly smaller values when required. To generate the pseudopotential of absorbing lithium, the $1s$ state was included in the core.

For each compound, the supercell size convergence was verified, leading to the supercell parameters described in Table I. All the self-consistent-field (SCF) calculations were carried out with an energy cutoff for the electronic wave function and the density of 100 and 800 Ry, respectively, and a uniform Monkhorst-Pack $3 \times 3 \times 3$ k-point grid [75]. A $4 \times 4 \times 4$ k-point grid was used for the spectral calculations.

2. The core wave-function issue

The dynamic structure factor calculation for the monopole transition requires the evaluation of the radial part of the matrix element $\langle \psi_f | \, j_0(qr) \, | \psi_{1s} \rangle$. For low-$q$ values, $j_0(qr)$ tends to 1 and therefore $\lim_{q \to 0} \langle \psi_f | \, j_0(qr) \, | \psi_{1s} \rangle = 0$, as a consequence of the one-electron state orthogonality. Hence, the $S_{\text{mono}}(q, \omega)$ term is expected to vanish when q tends to 0.

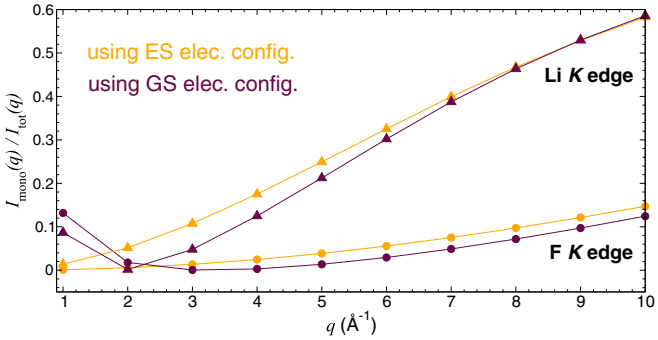

FIG. 2. Variation of $I_{\rm mono}(q)/I_{\rm tot}(q)$ as a function of q in the case of LiF (triangles for the Li K edge, circles for the F K edge). The I quantity corresponds to the dynamic structure factor $S(q,\omega)$ integrated over a 50 eV energy range ($I_{\rm mono}$ is the contribution of the monopole term only, $I_{\rm tot}$ is the integral of the sum of both monopole and dipole terms). Two electronic configurations of the absorbing atom were used to generate the atomic initial-state core wave function $R_{10\sigma}(r)$—the ground-state (GS) one and the excited-state (ES) one—which was obtained with only one $1s$ electron.

In our pseudopotential scheme, the evaluation of the radial part of $\langle\psi_f|\, j_0(qr)\,|\psi_{1s}\rangle$ requires the calculation of integrals defined by Eq. (9). In XSPECTRA, initially developed for x-ray absorption calculations in which monopole electronic transitions are forbidden, the radial parts of the absorbing atom core-state partial wave, $R_{10\sigma}(r)$ for a K edge, and the absorbing atom final-state partial wave, $R_{p\ell\sigma}(r)$, are usually extracted from ground-state and excited-state electronic configurations, respectively, and are therefore not orthogonal. For XRS calculations, as a consequence of this loss of orthogonality, the monopole intensity for very low q values rises again instead of vanishing, as shown in Fig. 2 in the case of LiF. The simplest way to circumvent this issue consists in using an atomic radial core wave function calculated for an excited-state electronic configuration of the absorbing atom. By doing so, the orthogonality between the initial and final states is restored, so that the monopole signal monotonically decreases with the q-value, as it should (see Fig. 2). Whereas at the F K edge, the $I_{\rm mono}(q)/I_{\rm tot}(q)$ ratio obtained using both radial core wave functions differs by a few percent over the full range of q values, they converge to the same value at the Li K edge in the high-q limit.

3. Isotropic dynamic structure factor calculation

For dipole transitions, the isotropic dynamic structure factor of $LiBO_2$ and $LiCO_3$ was obtained by the mean average of $S_{\rm dip}(\boldsymbol{q},\omega)$ calculated with three distinct orientations: $\boldsymbol{q} \parallel [100]$, $\boldsymbol{q} \parallel [010]$, and $\boldsymbol{q} \parallel [001]$. Since dipole transitions are isotropic for cubic structures, the isotropic dynamic structure factor of Li_2O and LiF was obtained by using only one of the three above-mentioned $\boldsymbol{q}$-orientations.

For quadrupole transitions, the isotropic dynamic structure factor of cubic structures can be expressed as

$$S^{\rm iso}_{\rm quad}(q,\omega) = \tfrac{1}{5}[S_{\rm quad}(\boldsymbol{q} \parallel [100],\omega) + 4S_{\rm quad}(\boldsymbol{q} \parallel [110],\omega)]. \quad (13)$$

Equation (13) was used in the case of Li_2O and LiF. $S^{\rm quad}_{\rm iso}(q,\omega)$ was not calculated for the crystals with lower symmetries, i.e., the monoclinic structures $LiBO_2$ and Li_2CO_3 since their quadrupole contributions were found to be two orders of magnitude smaller than the monopole and dipole terms in the energy range of interest (see Sec. IV C).

4. Core-level shift calculation

In $LiBO_2$ and Li_2CO_3, oxygen occupies two inequivalent crystallographic sites, leading to two distinct theoretical spectra that have to be weighted appropriately. Before averaging, the two individual spectra are energy-shifted using the ΔSCF approach described in Ref. [49], which we briefly summarize here for completeness.

In a first step, the energies of the lowest unoccupied electronic state, $\epsilon_{\rm lumo}$, of individual spectra calculated in FCH or XCH, depending on the approximation selected for the element under consideration, are set to the same value. In a second step, the relative excitation energies are evaluated as the differences of supercell total energies obtained in the XCH approximation, $E_{\rm XCH}$, i.e., by promoting the photoelectron from the core state to the lowest available conduction state. Assuming a reference site i, the relative position of the component arising from site j is therefore obtained as

$$\begin{aligned}\Delta^j_{\rm CLS} &= E^j_{\rm XCH} - E^i_{\rm XCH} + \epsilon^i_{\rm lumo} - \epsilon^j_{\rm lumo} \\ &= \left(E^j_{\rm XCH} - \epsilon^j_{\rm lumo}\right) - \left(E^i_{\rm XCH} - \epsilon^i_{\rm lumo}\right). \end{aligned} \quad (14)$$

5. Spectral broadening and normalization

The continued fraction was calculated with the following energy-dependent broadening parameter $\gamma(E)$ [76]:

$$\gamma(E) = \Gamma_{\rm H} + \frac{\Gamma_{\rm M}}{2} + \frac{\Gamma_{\rm M}}{\pi}\arctan\left[\frac{\pi}{3}\frac{\Gamma_{\rm M}}{A_{\rm w}}\left(x - \frac{1}{x^2}\right)\right], \quad (15)$$

where $x = (E - E_F)/A_c$, E_F is the Fermi energy, and $\Gamma_{\rm H}$ is the core-hole finite lifetime broadening. The following set of values was used: $\Gamma_{\rm H} = 0.2$ eV, $\Gamma_{\rm M} = 3$ eV at the Li K edge and $\Gamma_{\rm M} = 5$ eV at the B, C, O, and F K edges, $A_{\rm c} = 30$ eV, and $A_{\rm w} = 30$ eV. A subsequent convolution by a Gaussian was performed to account for the experimental resolution. The same rigid energy shift, at low and high q, was applied to all the calculated spectra to match with experiment. The normalization procedure for spectra calculated with different values of q is the same as that for the experimental spectra, i.e., the integrated intensity of $S^{\rm iso}_{\rm tot}(q,\omega)$ was normalized to unity over the same energy range as the one used to normalize the integrated intensity of the corresponding experimental XRS spectrum.

IV. RESULTS AND DISCUSSION

A. Comparison between experiments and calculations

In Fig. 3, the experimental XRS spectra for $LiBO_2$, Li_2CO_3, Li_2O, and LiF acquired for two values of q are compared with the corresponding calculated spectra. For all K edges, a good agreement is observed, with a well-reproduced q-dependence. Nevertheless, calculated spectral features systematically appear to be slightly contracted when compared with the experiments. For instance, the second peak of the Li

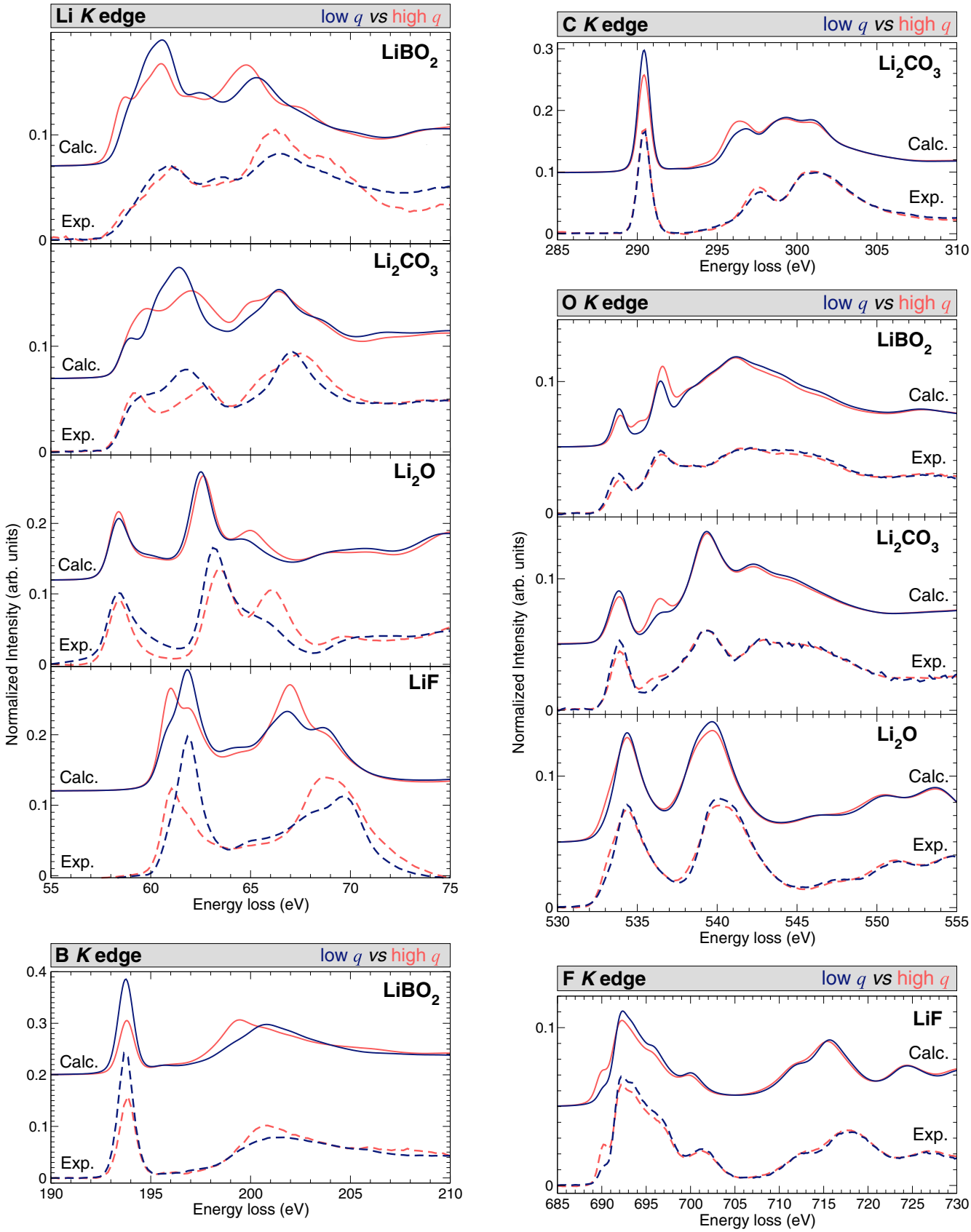

FIG. 3. Comparison between experimental and calculated XRS spectra for $LiBO_2$, Li_2CO_3, Li_2O, and LiF at low q (4.5 $Å^{-1}$) and high q (8.5 $Å^{-1}$), except for $LiBO_2$ (low $q = 2.4$ $Å^{-1}$, high $q = 10.2$ $Å^{-1}$). The XCH approximation is used for Li, B, and C while FCH is used for O and F. The calculated spectra are shifted vertically for clarity.

K-edge theoretical spectrum in Li_2O at low q is downshifted by about 0.5 eV with respect to the experiments, and this contraction tends to be more pronounced as the energy increases. This discrepancy, which is known to be related to the use of DFT, tends to underestimate the gap and the energies of the empty states [55,77,78].

In the following, the spectra are analyzed and discussed according to the probed element.

1. Li K edge

As shown in Fig. 3, Li *K*-edge XRS spectra strongly depend on the compound. As XRS is sensitive to the local environment of the absorbing atom, the observed spectral similarities/differences can be tentatively ascribed to some particular coordination geometries of the lithium polyhedron.

$LiBO_2$ and Li_2CO_3 spectra exhibit similar overall shapes: the Li local environments in $LiBO_2$ and Li_2CO_3 are comparable, although their crystal structures differ (infinite chains of triangular units BO_3 and isolated triangular CO_3, respectively, as shown in Fig. 1). In both cases, Li has four oxygen neighbors at about 1.96 Å, with, for $LiBO_2$, an additional neighbor at much longer distance (2.47 Å). In Li_2O, Li also has four oxygen first neighbors as it is located at the center of a regular tetrahedron ($d_{\text{Li-O}} = 2.0$ Å), but the shape of the spectrum strongly differs from those of $LiBO_2$ and Li_2CO_3. This emphasizes that the interpretation of the spectral shape solely in terms of local structure is rather limited. The overall shape of the LiF XRS spectrum significantly differs from that of the oxygen-bearing crystals, the most striking difference being the energy shift of the edge onset of 2 eV. This shift to higher energy, previously reported in Ref. [50], could be related, at least to some extent, to an increase of both the coordination number of Li [79,80] from $^{[4]}$Li in $LiBO_2$, Li_2CO_3, and Li_2O to $^{[6]}$Li in LiF and to an increase of the anion electronegativity from O to F [81,82].

For all compounds, the q-dependence is significant on an energy range extending over about 10 eV above the edge onset. This might simply be explained by the fact that, in an ionic picture, Li is formally close to Li^+ so that the first unoccupied Li 2*s* states dominate the bottom of the conduction band. Therefore, at high q, a strong signal arising from monopole transitions is expected due to a large density of unoccupied 2*s* states [50]. The q-dependence, as observed here for LiF, Li_2CO_3, and Li_2O both experimentally and theoretically, is consistent with the results of Fister *et al.* [83].

2. B and C K edges

B and C *K*-edge spectra of $LiBO_2$ and Li_2CO_3 are analogous, because of the structural similarities of triangular BO_3 and CO_3 units (Figs. 1 and 3). Both spectra can be decomposed in a narrow and intense first peak corresponding to dipole transitions toward $\pi^\star$ out-of-plane antibonding states and a higher-lying broader structure associated with transitions to the unoccupied $\sigma^\star$ in-plane antibonding states [22,84]. The $\sigma^\star$ peak appears to be more structured in the carbonate than in the borate, which might be attributed to the presence of a double C=O bond in the former.

The C *K*-edge spectra of Li_2CO_3 display a weak dependence with q, the main effect being limited to a slight increase of the first peak of the $\sigma^\star$ structure with q. Our calculations reproduce this effect, but also exhibit an opposite q-dependence of the $\pi^\star$-peak intensity, in agreement with the experimental XRS spectra of Fister *et al.* [83]. Even though the spectra have been recorded under slightly different experimental conditions, exploring a wider q range for $LiBO_2$, the B *K* edge, and more precisely the relative intensity of the $\pi^\star$ and the $\sigma^\star$ structures, seems to be more sensitive to the norm of the momentum transfer. This intensity ratio can be reduced by a factor of about 1.5–2 when moving from the low-q (2.4 Å^{-1}) to the high-q region (10.2 Å^{-1}).

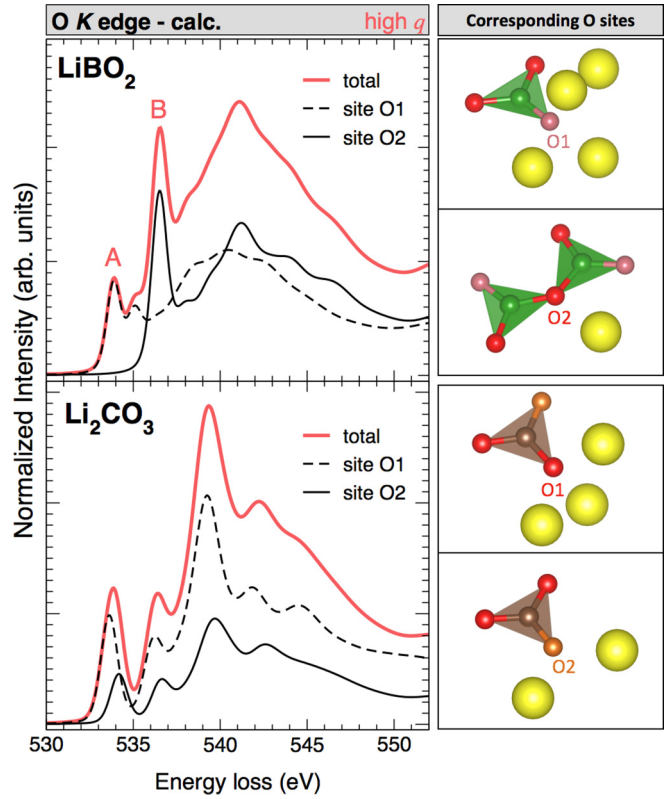

FIG. 4. Decomposition of the calculated O *K*-edge XRS spectrum at high q into oxygen-site-dependent contributions for $LiBO_2$ (top, $q = 10.2$ Å^{-1}) and Li_2CO_3 (bottom, $q = 8.5$ Å^{-1}). For each crystal, the local environment within a 3 Å radius cluster of the two oxygen nonequivalent sites, labeled O1 and O2, is displayed on the right. FCH approximation is used.

3. O K edge

The overall O *K*-edge spectral shapes of $LiBO_2$ and Li_2CO_3 are similar, as compared to that of Li_2O. This is in line with the similarities observed in the Li, B, and C *K*-edge spectra described previously. Unlike Li_2O, for which a unique oxygen site is reported, the crystal structures of $LiBO_2$ and Li_2CO_3 both contain two nonequivalent oxygen sites leading to a more complex structure in the O *K*-edge spectra. These two O sites, which show two distinct coordination numbers $^{[3]}$O and $^{[4]}$O, are involved in covalent (O-B or O-C) or in more ionic bonds (O-Li). Consequently, they are characterized by rather different local electronic structures. DFT calculations provide the individual contributions associated with each nonequivalent oxygen atom (see Fig. 4). For $LiBO_2$, the A peak observed at 534 eV arises from transitions to the oxygen

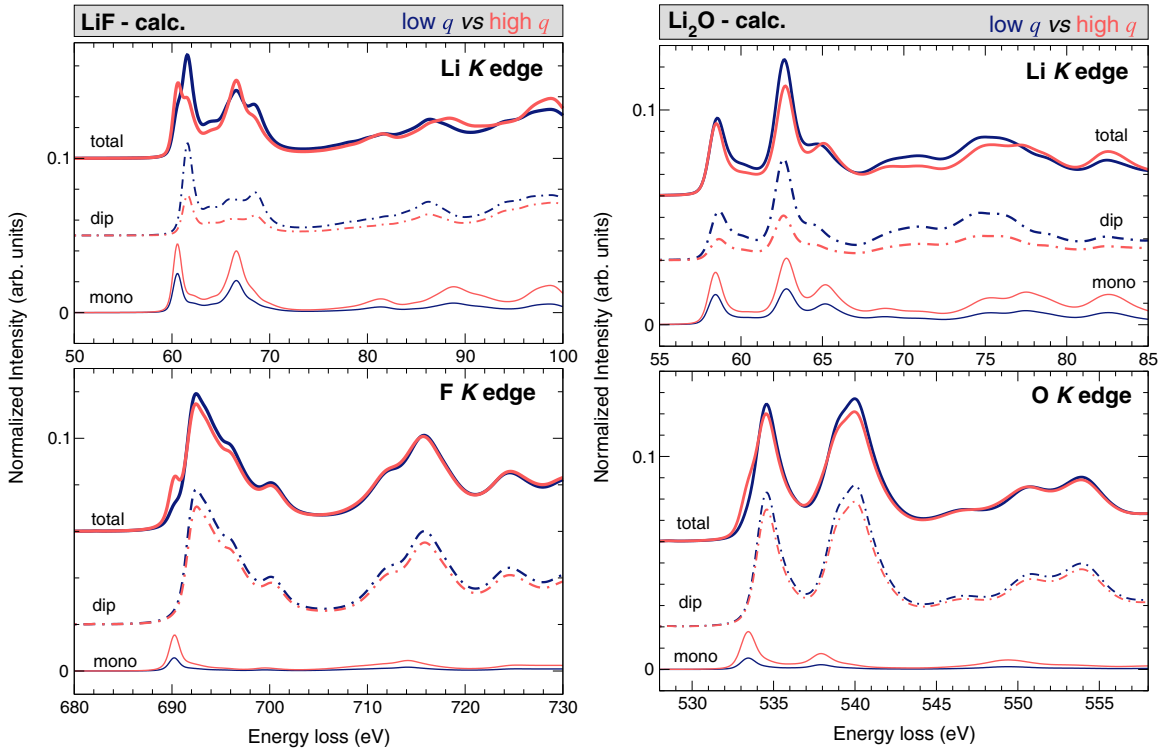

FIG. 5. Decomposition of the calculated XRS spectra (thick solid line) of LiF (left) and Li_2O (right) into monopole (dashed-dotted line) and dipole (thin solid line) contributions, for $q = 4.5$ Å^{-1} (low q) and $q = 8.5$ Å^{-1} (high q), plotted over a 50 eV (30 eV) energy range for LiF (Li_2O). The total spectra and dipole contributions are shifted vertically for clarity. The XCH approximation is used for Li, while FCH is used for O and F.

component of the $\pi^\star$ states of the BO_3 structural units and is associated with nonbridging oxygen atoms, whereas the B peak located at 536.5 eV is related to transitions toward the same antibonding states but associated with bridging oxygen atoms [49]. The two nonequivalent oxygen sites (O1 and O2) in Li_2CO_3 lead to similar spectral features, but separated by a core-level shift of about 0.7 eV only, which is much smaller than in the case of $LiBO_2$ (slightly more than 2.0 eV). Indeed, as is visible in the 3 Å radius clusters shown in Fig. 4, O1 and O2 share very similar local environments in Li_2CO_3, in sharp contrast with $LiBO_2$.

Figure 3 shows that the q-dependence of the O K-edge XRS spectra is more subtle than that of the Li or B K-edge spectra (see Sec. IV A 2) and has even been omitted in previous XRS studies [83] of Li_2O and Li_2CO_3. The weak q-dependence is especially clear in the case of Li_2O, where, with the exception of the growth of a small excitonic shoulder right below the edge onset (∼533 eV) similar to what is observed in the F K-edge spectra of LiF (see Sec. IV A 4 below), the general shape of the spectra remains otherwise largely unchanged. The q-dependence of O K-edge XRS spectra of $LiBO_2$ and Li_2CO_3 is almost the same and involves the spectral region related to the $\pi^\star$ antibonding states. Even though they are weak, these spectral differences with q are rather nicely reproduced by the calculations.

4. F K edge

At the F K edge, the q-dependence is primarily seen in a feature at 690 eV that grows with q and is attributed to monopole transitions. These results are consistent with previously reported studies [39,40,51,83], the remaining discrepancies coming from the choice of spectral normalization. The first experimental evidence of the q-dependence of the F K-edge XRS spectrum was reported by Hämäläinen *et al.* [39] for q varying from 2.72 to 10.20 Å^{-1}, and later confirmed by Fister *et al.* [83] (q ranging from 1.3 to 7.8 Å^{-1}) and by Joly *et al.* [40] (q ranging from 3.14 to 8.72 Å^{-1}). The q-dependence is well reproduced by the calculations performed using either a single-particle DFT framework (this study and Ref. [40]) or a two-particle approach based on the Bethe-Salpeter equation (BSE) [39,51,83]. For a high q value, a more in-depth comparison between both calculation methods is presented in Sec. IV C.

B. Monopole versus dipole transitions

A systematic decomposition of the q-dependent XRS spectra in terms of monopole and dipole transitions is presented in Fig. 5 for LiF and Li_2O and in Fig. 6 for $LiBO_2$ and Li_2CO_3. As already noted in Sec. IV A 1, monopole transitions bring a large contribution to the spectral shape at the Li K edge and may even completely dominate the dipole contribution for sufficiently large momentum transfers. This peculiarity arises from the fact that the 2s states of the Li^+ ion strongly contribute to the low-lying unoccupied states in lithium-bearing compounds.

As monopole transitions are closely related to the local s projected density of states, they strongly depend on the

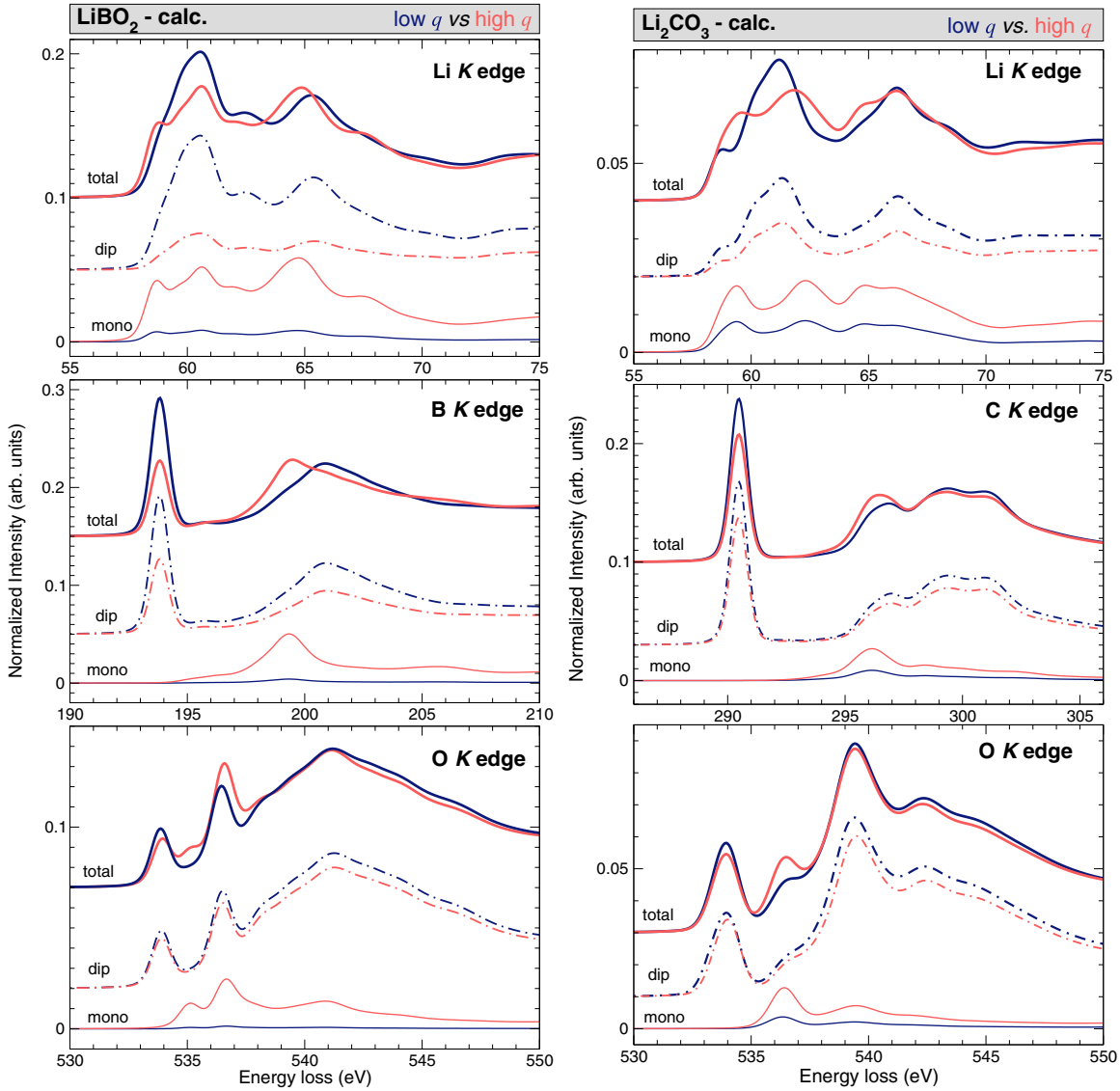

FIG. 6. Decomposition of the calculated XRS spectra (thick solid line) of $LiBO_2$ (left) and Li_2CO_3 (right), into monopole (dashed-dotted line) and dipole (thin solid line) contributions, for both low and high q values (2.4 and 10.2 $Å^{-1}$ for $LiBO_2$, 4.5 and 8.5 $Å^{-1}$ for Li_2CO_3). The XCH approximation is used for Li, B, and C, while FCH is used for O. The spectra are plotted over a 20 eV energy range. The total spectra and dipole contributions are shifted vertically for clarity.

local environment of the excited atom, i.e., the nature of the chemical bonds between the probed atom and its neighbors or the local symmetry. For instance, in $LiBO_2$ and Li_2CO_3 (see Fig. 6), B and C atoms are, respectively, at the center of planar triangular BO_3 and CO_3 structural units favoring the formation of in-plane σ covalent bonds involving sp^2 hybrids. On the contrary, out-of-plane π bonds purely involve p states. As a consequence, monopole transitions are predominantly contributing to the high-lying $\sigma^\star$ peak in the B and C K edges. The same remarks apply to the O K edge in $LiBO_2$ and Li_2CO_3 as their shape echoes the same underlying electronic structure. Their analysis is, however, less straightforward due to the overlapping contributions of the two inequivalent sites. Finally, in ionic compounds like LiF and Li_2O (see Fig. 5), monopole contributions at anion K edges are very sensitive to the presence of the core hole and give rise to spectral features essentially localized at the edge onset, which displays a strong excitonic character.

C. Core-hole electron interaction modeling

In a DFT supercell framework, several approximations can be used to model the core-hole electron interaction, such as FCH, XCH, and HCH (see Sec. III C 1). Beyond DFT, the core-hole electron interaction can be modeled using a two-particle picture within a many-body perturbation theory framework, as described by the Bethe-Salpeter equation (BSE). Figure 7 (top panel) presents a systematic comparison of these approximations with the experimental spectrum of the Li K edge in LiF for the high q value, including a decomposition in terms of monopole, dipole, and quadrupole contributions. The BSE calculations were performed using the OCEAN package [52], starting with a DFT ground-state electronic structure generated in the local density approximation (LDA) using QUANTUM ESPRESSO. All the spectra were broadened and normalized using the same parameters (see Sec. III C 5). As can be clearly observed, the calculated spectra strongly

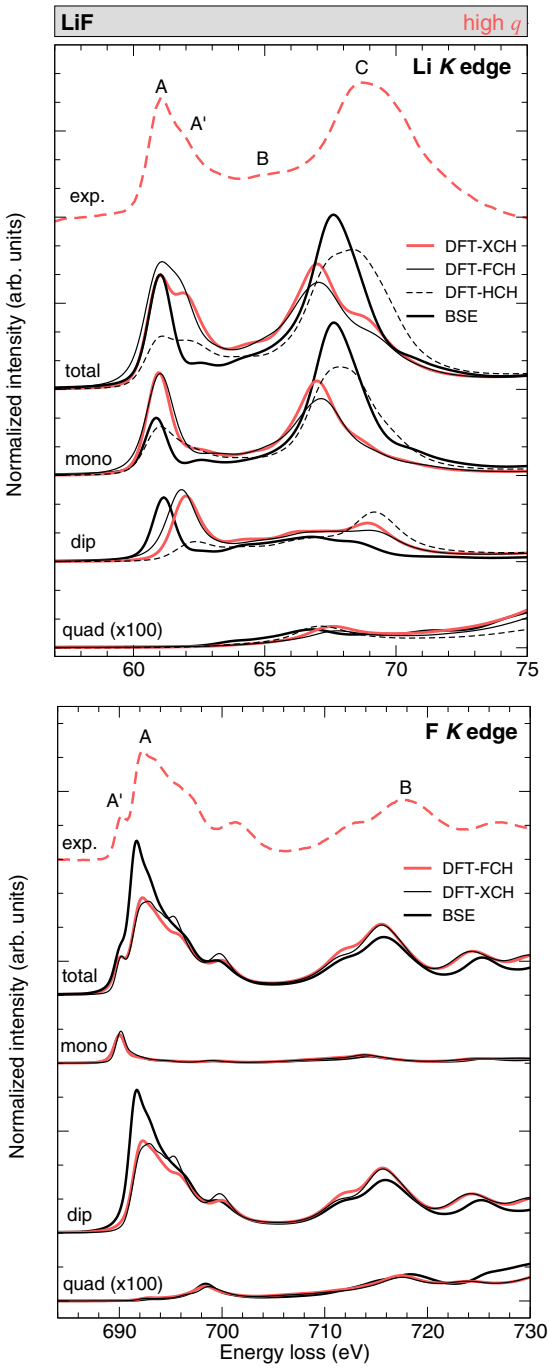

FIG. 7. Comparison between experimental and calculated XRS spectra for LiF at high q (8.5 Å^{-1}). The theoretical spectra are obtained using different models for the core-hole electron interaction: DFT using the FCH, XCH, and HCH approaches, and BSE as implemented in the OCEAN code. The calculated spectra were energy-shifted so as to align the first peak with experiment (peak A for the Li K edge and peak A′ for the F K edge). The total calculated spectra are decomposed into monopole, dipole, and quadrupole components. The spectra are vertically shifted for clarity.

depend on the approximation employed, which makes this very light element K edge a critical test case for the *ab initio* modeling of the core-hole electron interaction.

Most of the K-edge calculations carried out previously using XSPECTRA were performed within the FCH approximation [85–87], even in the case of light elements such as oxygen [49,88]. However, accounting for the core-hole effects in the framework of DFT still remains an open issue [89], and other approximations such as the XCH approach have also been employed [70]. In the present case of the Li K edge, the XCH calculation was indeed preferred over the FCH calculation as it permits us to better reproduce exciton peaks A and A′ as well as peak B and the relative intensities between peak A and the broad structure C. For analogous reasons, the XCH approach was chosen for all Li, B, and C K-edge XRS calculations presented in this work, although only a slight improvement was observed for the latter two elements.

The BSE calculation improves the agreement with experiments in terms of relative energy positions of the spectral features. More surprisingly, the same kind of improvement is also observed using the HCH approach, suggesting that relative energy positions are very sensitive to the core-hole electron interaction. The HCH approach provides the best result for the shape of peak C, but at the expense of the agreement with the A-A′ double structure, whose intensity is drastically underestimated within this approximation. Alternatively, the BSE approach tends to overestimate the intensity of peak C with respect to that of peak A, in agreement with previously reported BSE calculations of Li K-edge XRS spectra [83].

An interesting aspect of this comparison consists in assessing the capability of each approximation to describe the double A-A′ structure. As it is now well established [53], this structure is composed of a low-lying even-parity, or dipole-forbidden, exciton peak A and a higher-lying odd-parity, or dipole-allowed, exciton peak A′. These two peaks indeed clearly appear in distinct components of the spectrum, namely the monopole and dipole, respectively, revealing the different spatial symmetries of these excitations. As already noticed in the literature [53], the BSE calculation largely underestimates the energy separation of these two structures by predicting a splitting of about 0.28 eV, whereas it is experimentally close to 0.74 eV. Interestingly, single-particle DFT-based approaches are also able to capture these subtle excitonic signatures. The calculated A-A′ splitting, however, proves to be very sensitive to the way the core hole and its screening by the valence electrons are taken into account, varying from 1.26 eV in the HCH approach to 1.09 eV for the XCH and 0.84 eV for the FCH approximations.

As shown in the bottom panel of Fig. 7, the F K edge in LiF is not as sensitive to core-hole electron modeling as the Li K edge. FCH and XCH approaches lead to almost identical results, though a slightly better agreement with experiment is obtained in the region of peak A using the FCH approach. As in the case of the Li K edge, BSE calculations provide partial improvement in the relative energy positions of the spectral features, but they tend to overestimate the intensity of peak A with respect to higher-lying structure B. At the F K edge, our DFT and BSE calculations lead to almost superimposable monopole contributions that display a localized exciton peak at the origin of A′. The rest of the spectrum is largely dominated by dipole transitions. The quadrupole component is found negligible as in the case of the Li K edge.

Note that, in principle, as these experiments were carried out at room temperature, thermal effects should be included in

the calculations. Indeed, temperature induces symmetry lowering associated with nuclear displacements, which may result in hybridization of local electronic states and enable transitions that would otherwise be symmetry-forbidden. A number of studies focused on K edges recorded in XAS [87,90–92] or low-q XRS [50] show that an increase of the temperature not only leads to a general broadening of the line shapes but also enhances and shifts certain spectral features, especially in the pre-edge region. In this latter case, thermal fluctuations induce an admixture of local p character in otherwise s-like electronic states, at the origin of these apparently forbidden monopole transitions. Temperature effects may therefore be of importance when a quantitative interpretation of K pre-edge features is needed, as they might indeed enhance electronic transitions similar to those induced by the monopole term in finite-q experiments.

V. CONCLUSION

In summary, we have presented an efficient method for calculating K edges in x-ray Raman scattering spectroscopy developed in the framework of a single-particle theory and designed to fully account for the multipole transitions observed in finite-q experiments. The calculation of the dynamic structure factor is implemented in the framework of density functional theory, based on the pseudopotential-plane-wave method and on a recursive approach, avoiding the explicit calculation of high-lying unoccupied electronic states. This method is therefore particularly well suited to dealing with large systems of hundreds of atoms, such as complex minerals, liquids, or glasses. Our implementation has been validated using an extensive set of edges recorded in a series of reference lithium-bearing compounds, and it proves to be very useful for analyzing XRS spectra beyond the dipole approximation.

Further important developments include the extension of this method to the modeling of the $L_{2,3}$ edges of light elements easily accessible in XRS for which additional difficulties arise from the multiple transition channels already present in the dipole term and where subtle effects are expected to result from the shallow core-hole electron interaction. Inclusion of temperature effects also appear as an essential step toward a quantitative modeling of this technique, frequently employed in the context of *in situ* experiments. In particular, accounting for the effects of thermal fluctuations on the theoretical spectra is crucial to disentangle the influence of temperature from the inherent monopole transitions observed in experiments carried out with a finite momentum transfer.

ACKNOWLEDGMENTS

For this work, access was granted to the HPC resources of IDRIS under the allocation 2017096863 made by GENCI (Grand Equipement National de Calcul Intensif). This work was supported by French state funds managed by the ANR within the Investissements d'Avenir programme under reference ANR-11-IDEX-0004-02, and more specifically within the framework of the Cluster of Excellence MATISSE led by Sorbonne Universités. We acknowledge the ESRF for providing synchrotron radiation and technical support.

APPENDIX: COMPARISON BETWEEN XAS AND XRS

Following the notations used in this paper, the XAS cross section reads

$$\sigma(\omega) = 4\pi^2\alpha_0\hbar\omega \sum_f |\langle\psi_f|O^{\rm XAS}|\psi_i\rangle|^2\delta(E_f - E_i - \hbar\omega), \tag{A1}$$

where α_0 is the fine-structure constant, $\hbar\omega$ is the energy of the incident (absorbed) photon, and $O^{\rm XAS}$ is the XAS transition operator. In the electric quadrupole approximation, $O^{\rm XAS}$ is the sum of two terms, namely the electric dipole and the electric quadrupole terms (usually labeled E1 and E2, respectively),

$$O^{\rm XAS}_{\rm dip} = \hat{\varepsilon}\cdot\boldsymbol{r}, \tag{A2}$$

$$O^{\rm XAS}_{\rm quad} = \frac{i}{2}\,\hat{\varepsilon}\cdot\boldsymbol{r}\,\boldsymbol{k}\cdot\boldsymbol{r}, \tag{A3}$$

where $\hat{\varepsilon}$ and $\boldsymbol{k}$ are the polarization unit vector and the wave vector of the incident x-ray beam, respectively. Expressing the scalar products with spherical harmonics and using $\boldsymbol{r} = r\hat{r}$ and $\boldsymbol{k} = k\hat{k}$, Eqs. (A2) and (A3) become

$$O^{\rm XAS}_{\rm dip} = r\,\frac{4\pi}{3}\sum_\lambda (-1)^\lambda Y_1^{-\lambda}(\hat{\varepsilon})Y_1^\lambda(\hat{r}), \tag{A4}$$

$$O^{\rm XAS}_{\rm quad} = r^2\,k\frac{4i\pi\sqrt{2\pi}}{3\sqrt{15}}\sum_{\lambda,\mu} Y_1^{-\lambda}(\hat{\varepsilon})Y_1^{-\mu}(\hat{k}) \times\sum_\nu (-1)^\nu(1\lambda1\mu|2\nu)Y_2^\nu(\hat{r}). \tag{A5}$$

In Eq. (A5), $(1\lambda1\mu|2\nu)$ is a Clebsch-Gordan coefficient. The electric dipole transitions are the leading contribution and, in most cases, the only observable transitions. The electric quadrupole transitions are essentially visible at the K pre-edge of $3d$ transition elements [85].

The dynamic structure factor reads

$$S(\boldsymbol{q},\omega) = \sum_f |\,\langle\psi_f|\,O^{\rm XRS}\,|\psi_i\rangle\,|^2\delta(E_f - E_i - \hbar\omega), \tag{A6}$$

where the XRS transition operator is given by

$$O^{\rm XRS} = e^{i\boldsymbol{q}\cdot\boldsymbol{r}}. \tag{A7}$$

$O^{\rm XRS}$ can be expanded in terms of spherical harmonics using Bauer's identity [Eq. (4)], which, up to second order, leads to the following three terms:

$$O^{\rm XRS}_{\rm mono} = j_0(qr), \tag{A8}$$

$$O^{\rm XRS}_{\rm dip} = j_1(qr)4i\pi\sum_\lambda (-1)^\lambda Y_1^{-\lambda}(\hat{q})Y_1^\lambda(\hat{r}), \tag{A9}$$

$$O^{\rm XRS}_{\rm quad} = -j_2(qr)4\pi\sum_\nu (-1)^\nu Y_2^{-\nu}(\hat{q})Y_2^\nu(\hat{r}). \tag{A10}$$

In the limit of small momentum transfers, i.e., if $qr \ll 1$, only terms up to the first order in qr can be kept in the Taylor

series of spherical Bessel functions [93] $j_\lambda(qr)$,

$$j_\lambda(qr) = \sum_{k=0}^{\infty} \frac{(-1)^k}{2^k k!(2k+2\lambda+1)!!}(qr)^{2k+\lambda}.$$

In this approximation, the XRS transition operator then reduces to only two terms,

$$O^{\mathrm{XRS}}_{\mathrm{mono}} \approx 1, \tag{A11}$$

$$O^{\mathrm{XRS}}_{\mathrm{dip}} \approx rq\frac{4i\pi}{3}\sum_{\lambda}(-1)^\lambda Y_1^{-\lambda}(\hat{q})Y_1^{\lambda}(\hat{r}). \tag{A12}$$

As $|\psi_f\rangle$ final and $|\psi_i\rangle$ initial states are assumed to be orthogonal, Eq. (A11) leads to zero transition-matrix element, and an XRS spectrum is mainly due to dipole transitions.

To conclude, in the $qr \ll 1$ limit, the XAS and XRS dipole transition operators only differ by the iq prefactor and by the interchange of $\hat{\varepsilon}$ and $\hat{q}$.

[1] T. Suzuki, J. Phys. Soc. Jpn. **22**, 1139 (1967).
[2] T. Suzuki, T. Kishimoto, T. Kaji, and T. Suzuki, J. Phys. Soc. Jpn. **29**, 730 (1970).
[3] K. Tohji and Y. Udagawa, Phys. Rev. B **36**, 9410(R) (1987).
[4] Y. Feng, G. T. Seidler, J. O. Cross, A. T. Macrander, and J. J. Rehr, Phys. Rev. B **69**, 125402 (2004).
[5] Y. Feng, J. A. Soininen, A. L. Ankudinov, J. O. Cross, G. T. Seidler, A. T. Macrander, J. J. Rehr, and E. L. Shirley, Phys. Rev. B **77**, 165202 (2008).
[6] P. Wernet, D. Nordlund, U. Bergmann, M. Cavalleri, M. Odelius, H. Ogasawara, L. A. Näslund, T. K. Hrisch, L. Ojamäe, P. Glatzel, L. G. M. Pettersson, and A. Nilsson, Science **304**, 995 (2004).
[7] T. Pylkkänen, J. Lehtola, H. Hakala, A. Sakko, G. Monaco, S. Huotari, and K. Hämäläinen, J. Phys. Chem. B **114**, 13076 (2010).
[8] I. Juurinen, T. Pylkkänen, K. O. Ruotsalainen, C. J. Sahle, G. Monaco, K. Hämäläinen, S. Huotari, and M. Hakala, J. Phys. Chem. B **117**, 16506 (2013).
[9] A. Sakko, S. Galambosi, J. Inkinen, T. Pylkkänen, M. Hakala, S. Huotari, and K. Hämäläinen, Phys. Chem. Chem. Phys. **13**, 11678 (2011).
[10] J. Inkinen, A. Sakko, K. O. Ruotsalainen, T. Pylkkänen, J. Niskanen, S. Galambosi, M. Hakala, G. Monaco, S. Huotari, and K. Hämäläinen, Phys. Chem. Chem. Phys. **15**, 9231 (2013).
[11] Y. Mizuno and Y. Ohmura, J. Phys. Soc. Jpn. **22**, 445 (1967).
[12] W. Schülke, *Electron Dynamics by Inelastic X-ray Scattering*, Oxford Series on Synchrotron Radiation No. 7 (Oxford University Press, Oxford, 2007).
[13] W. L. Mao, H.-K. Mao, P. J. Eng, T. P. Trainor, M. Newville, C. Kao, D. L. Heinz, J. Shu, Y. Meng, and R. J. Hemley, Science **302**, 425 (2003).
[14] Y. Meng, H.-K. Mao, P. J. Eng, T. P. Trainor, M. Newville, M. Y. Hu, C. Kao, J. Shu, R. J. Hausermann, and D Hemley, Nat. Mater. **3**, 111 (2004).
[15] J. S. Tse, M. Hanfland, R. Flacau, S. Desgreniers, Z. Li, K. Mende, K. Gilmore, A. Nyrow, M. Moretti Sala, and C. Sternemann, J. Phys. Chem. C **118**, 1161 (2014).
[16] J.-F. Lin, H. Fukui, D. Prendergast, T. Okuchi, Y. Q. Cai, N. Hiraoka, C.-S. Yoo, A. Trave, P. Eng, M. Y. Hu, and P. Chow, Phys. Rev. B **75**, 012201 (2007).
[17] H. Fukui, M. Kanzaki, N. Hiraoka, and Y. Q. Cai, Phys. Rev. B **78**, 012203 (2008).
[18] M. Wu, Y. Liang, J.-Z. Jiang, and J. S. Tse, Sci. Rep. **2**, 398 (2012).
[19] S. K. Lee, J.-F. Lin, Y. Q. Cai, N. Hiraoka, P. J. Eng, T. Okuchi, H.-K. Mao, Y. Meng, M. Y. Hu, P. Chow, J. Shu, B. Li, H. Fukui, B. H. Lee, H. N. Kim, and C.-S. Yoo, Proc. Natl. Acad. Sci. (U.S.A.) **105**, 7925 (2008).
[20] B. J. A. Moulton, G. S. Henderson, H. Fukui, N. Hiraoka, D. de Ligny, C. Sonneville, and M. Kanzaki, Geoch. Cosmoch. Acta **178**, 41 (2016).
[21] G. Lelong, L. Cormier, G. Ferlat, V. Giordano, G. S. Henderson, A. Shukla, and G. Calas, Phys. Rev. B **85**, 134202 (2012).
[22] S. K. Lee, P. J. Eng, H.-K. Mao, Y. Meng, M. Newville, M. Y. Hu, and J. Shu, Nat. Mater. **4**, 851 (2005).
[23] S. K. Lee, P. J. Eng, H.-K. Mao, Y. Meng, and J. Shu, Phys. Rev. Lett. **98**, 105502 (2007).
[24] Y. Q. Cai, H.-K. Mao, P. C. Chow, J. S. Tse, Y. Ma, S. Patchkovskii, J. F. Shu, V. Struzhkin, R. J. Hemley, H. Ishii, C. C. Chen, I. Jarrige, C. T. Chen, S. R. Shieh, E. P. Huang, and C. C. Kao, Phys. Rev. Lett. **94**, 025502 (2005).
[25] T. Pylkkänen, V. M. Giordano, J.-C. Chervin, A. Sakko, M. Hakala, J. A. Soininen, K. Hämäläinen, G. Monaco, and S. Huotari, J. Phys. Chem. B **114**, 3804 (2010).
[26] C. J. Sahle, C. Sternemann, C. Schmidt, S. Lehtola, S. Jahn, L. Simonelli, S. Huotari, M. Hakala, T. Pylkkänen, A. Nyrow, K. Mende, M. Tolan, K. Hämäläinen, and M. Wilke, Proc. Natl. Acad. Sci. (U.S.A.) **110**, 6301 (2013).
[27] N. Watanabe, H. Hayashi, Y. Udagawa, K. Takeshita, and H. Kawata, Appl. Phys. Lett. **69**, 1370 (1996).
[28] A. Mattila, J. A. Soininen, S. Galambosi, S. Huotari, G. Vankó, N. D. Zhigadlo, J. Karpinski, and K. Hämäläinen, Phys. Rev. Lett. **94**, 247003 (2005).
[29] M. Moretti Sala, M. Rossi, A. Al-Zein, S. Boseggia, E. C. Hunter, R. S. Perry, D. Prabhakaran, A. T. Boothroyd, N. B. Brookes, D. F. McMorrow, G. Monaco, and M. Krisch, Phys. Rev. B **90**, 085126 (2014).
[30] T. Willers, F. Strigari, N. Hiraoka, Y. Q. Cai, M. W. Haverkort, K.-D. Tsuei, Y. F. Liao, S. Seiro, C. Geibel, F. Steglich, L. H. Tjeng, and A. Severing, Phys. Rev. Lett. **109**, 046401 (2012).
[31] J.-P. Rueff, J. M. Ablett, F. Strigari, M. Deppe, M. W. Haverkort, L. H. Tjeng, and A. Severing, Phys. Rev. B **91**, 201108(R) (2015).
[32] T. Suzuki and H. Nagasawa, J. Phys. Soc. Jpn. **39**, 1579 (1975).
[33] R. A. Gordon, G. T. Seidler, T. T. Fister, M. W. Haverkort, G. A. Sawatzky, A. Tanaka, and T. K. Sham, Europhys. Lett. **81**, 26004 (2008).
[34] J. A. Bradley, K. T. Moore, G. van der Laan, J. P. Bradley, and R. A. Gordon, Phys. Rev. B **84**, 205105 (2011).

[35] R. Cacuiffo, G. van der Laan, L. Simonelli, T. Vitova, C. Mazzoli, M. A. Denecke, and G. H. Lander, Phys. Rev. B **81**, 195104 (2010).

[36] S. Sen Gupta, J. A. Bradley, M. W. Haverkort, G. T. Seidler, A. Tanaka, and G. A. Sawatzky, Phys. Rev. B **84**, 075134 (2011).

[37] C. Sternemann, M. Volmer, J. A. Soininen, H. Nagasawa, M. Paulus, H. Enkisch, G. Schmidt, M. Tolan, and W. Schülke, Phys. Rev. B **68**, 035111 (2003).

[38] M. H. Krisch, F. Sette, C. Masciovecchio, and R. Verbeni, Phys. Rev. Lett. **78**, 2843 (1997).

[39] K. Hämäläinen, S. Galambosi, J. A. Soininen, E. L. Shirley, J.-P. Rueff, and A. Shukla, Phys. Rev. B **65**, 155111 (2002).

[40] Y. Joly, C. Cavallari, S. A. Guda, and C. J. Sahle, J. Chem. Theor. Comput. **13**, 2172 (2017).

[41] J. A. Soininen, A. Mattila, J. J. Rehr, S. Galambosi, and K. Hämäläinen, J. Phys.: Condens. Matter **18**, 7327 (2006).

[42] T. T. Fister, G. T. Seidler, E. L. Shirley, F. D. Vila, J. J. Rehr, K. P. Nagle, J. C. Linehan, and J. O. Cross, J. Chem. Phys. **129**, 044702 (2008).

[43] T. T. Fister, F. D. Vila, G. T. Seidler, L. Svec, J. C. Linehan, and J. O. Cross, J. Am. Chem. Soc. **130**, 925 (2007).

[44] G. van der Laan, Phys. Rev. B **86**, 035138 (2012).

[45] S. Huotari, E. Suljoti, C. J. Sahle, S. Rädel, G. Monaco, and F. M. F. de Groot, New J. Phys. **17**, 043041 (2015).

[46] J. A. Soininen, A. L. Ankudinov, and J. J. Rehr, Phys. Rev. B **72**, 045136 (2005).

[47] A. Sakko, M. Hakala, J. A. Soininen, and K. Hämäläinen, Phys. Rev. B **76**, 205115 (2007).

[48] J. Lehtola, M. Hakala, A. Sakko, and K. Hämäläinen, J. Comput. Chem. **33**, 1572 (2012).

[49] G. Lelong, G. Radtke, L. Cormier, H. Bricha, J.-P. Rueff, J. M. Ablett, D. Cabaret, F. Gélébart, and A. Shukla, Inorg. Chem. **53**, 10903 (2014).

[50] T. A. Pascal, U. Boesenberg, R. Kostecki, T. J. Richardson, T.-C. Weng, D. Sokaras, D. Nordlund, E. McDermott, A. Moewes, J. Cabana, and D. Prendergast, J. Chem. Phys. **140**, 034107 (2014).

[51] J. Vinson, J. J. Rehr, J. J. Kas, and E. L. Shirley, Phys. Rev. B **83**, 115106 (2011).

[52] K. Gilmore, J. Vinson, E. L. Shirley, D. Prendergast, C. D. Pemmaraju, J. J. Kas, F. D. Vila, and J. J. Rehr, Comput. Phys. Commun. **197**, 109 (2015).

[53] J. A. Soininen, K. Hämäläinen, W. A. Caliebe, C.-C. Kao, and E. L. Shirley, J. Phys.: Condens. Matter **13**, 8039 (2001).

[54] E. L. Shirley, Phys. Rev. Lett. **80**, 794 (1998).

[55] M. Taillefumier, D. Cabaret, A.-M. Flank, and F. Mauri, Phys. Rev. B **66**, 195107 (2002).

[56] C. Gougoussis, M. Calandra, A. P. Seitsonen, and F. Mauri, Phys. Rev. B **80**, 075102 (2009).

[57] O. Bunau and M. Calandra, Phys. Rev. B **87**, 205105 (2013).

[58] J.-P. Rueff and A. Shukla, Rev. Mod. Phys. **82**, 847 (2010).

[59] P. E. Blöchl, Phys. Rev. B **50**, 17953 (1994).

[60] C. Gougoussis, M. Calandra, A. Seitsonen, C. Brouder, A. Shukla, and F. Mauri, Phys. Rev. B **79**, 045118 (2009).

[61] W. H. Zachariasen, Acta Crystallogr. **17**, 749 (1964).

[62] J. Zemann, Acta Crystallogr. **10**, 664 (1957).

[63] R. W. G. Wyckoff, *Crystal Structures* (Wiley, New York, 1963), Vol. 1.

[64] H. Ott, Z. Krist. Cryst. Mat. **63**, 222 (1926).

[65] M. D. Mathews, A. K. Tyagi, and P. N. Moorthy, Thermochim. Acta **320**, 89 (1998).

[66] G. Lelong, L. Cormier, L. Hennet, F. Michel, J.-P. Rueff, J. M. Ablett, and G. Monaco, J. Non-Cryst. Solids **472**, 1 (2017).

[67] S. Huotari, C. J. Sahle, C. Henriquet, A. Al-Zein, K. Martel, L. Simonelli, R. Verbeni, H. Gonzalez, M.-C. Lagier, C. Ponchut, M. Moretti Sala, M. Krisch, and G. Monaco, J. Synch. Rad. **24**, 521 (2017).

[68] C. J. Sahle, A. Mirone, J. Niskanen, J. Inkinen, M. Krisch, and S. Huotari, J. Synch. Rad. **22**, 400 (2015).

[69] P. Giannozzi, S. Baroni, N. Bonini, M. Calandra, R. Car, C. Cavazzoni, D. Ceresoli, G. L. Chiarotti, M. Cococcioni, I. Dabo, A. Dal Corso, S. de Gironcoli, S. Fabris, G. Fratesi, R. Gebauer, U. Gerstmann, C. Gougoussis, A. Kokalj, M. Lazzeri, L. Martin-Samos, N. Marzari, F. Mauri, R. Mazzarello, S. Paolini, A. Pasquarello, L. Paulatto, C. Sbraccia, S. Scandolo, G. Sclauzero, A. P. Seitsonen, A. Smogunov, P. Umari, and R. M. Wentzcovitch, J. Phys.: Condens. Matter **21**, 395502 (2009).

[70] D. Prendergast and G. Galli, Phys. Rev. Lett. **96**, 215502 (2006).

[71] D. Vanderbilt, Phys. Rev. B **41**, 7892 (1990).

[72] A. Dal Corso, Comput. Mater. Sci. **95**, 337 (2014).

[73] A. M. Rappe, K. M. Rabe, E. Kaxiras, and J. D. Joannopoulos, Phys. Rev. B **41**, 1227 (1990).

[74] J. P. Perdew, K. Burke, and M. Ernzerhof, Phys. Rev. Lett. **77**, 3865 (1996).

[75] H. J. Monkhorst and J. D. Pack, Phys. Rev. B **13**, 5188 (1976).

[76] M. P. Seah and W. A. Dench, *Quantitative Electron Spectroscopy of Surfaces—A Standard Data Base for Electron Inelastic Mean Free Paths in Solids* (National Physical Laboratory, Division of Chemical Standards, 1978), Vol. 82.

[77] J. J. Kas, J. Vinson, N. Trcera, D. Cabaret, E. L. Shirley, and J. J. Rehr, J. Phys.: Conf. Ser. **190**, 012009 (2009).

[78] W. Olovsson, I. Tanaka, T. Mizogushi, P. Puschnig, and C. Ambrosch-Draxl, Phys. Rev. B **79**, 041102(R) (2009).

[79] N. Trcera, D. Cabaret, S. Rossano, F. Farges, A.-M. Flank, and P. Lagarde, Phys. Chem. Min. **36**, 241 (2009).

[80] D. Cabaret, S. Rossano, and N. Trcera, Appl. Phys. Lett. **102**, 196101 (2013).

[81] K. Handa, K. Kojima, K. Taniguchi, K. Ozutsumi, and S. Ikeda, Mem. SR Center Ritsumeikan Univ. **7**, 3 (2005).

[82] C. O'Shaughnessy, G. S. Henderson, B. J. A. Moulton, L. Zuin, and D. R. Neuville, J. Synch. Rad. **25**, 543 (2018).

[83] T. T. Fister, M. Wilke, P. Fenter, C. S. Johnson, M. D. Slater, M. K. Y. Chan, and E. L. Shirley, J. Chem. Phys. **135**, 224513 (2011).

[84] J. A. Brandes, S. Wirick, and C. Jacobsen, J. Synch. Rad. **17**, 676 (2010).

[85] D. Cabaret, A. Bordage, A. Juhin, M. Arfaoui, and E. Gaudry, Phys. Chem. Chem. Phys. **12**, 5619 (2010).

[86] D. Cabaret, N. Emery, C. Bellin, C. Hérold, P. Lagrange, F. Wilhelm, A. Rogalev, and G. Loupias, Phys. Rev. B **87**, 075108 (2013).

[87] R. Nemausat, C. Gervais, C. Brouder, N. Trcera, A. Bordage, C. Coelho-Diogo, P. Florian, A. Rakhmatullin, I. Errea,

L. Paulatto, M. Lazzeri, and D. Cabaret, Phys. Chem. Chem. Phys. **19**, 6246 (2017).

[88] D. Cabaret, F. Mauri, and G. S. Henderson, Phys. Rev. B **75**, 184205 (2007).

[89] V. Mauchamp, M. Jaouen, and P. Schattschneider, Phys. Rev. B **79**, 235106 (2009).

[90] D. Manuel, D. Cabaret, C. Brouder, P. Sainctavit, A. Bordage, and N. Trcera, Phys. Rev. B **85**, 224108 (2012).

[91] R. Nemausat, D. Cabaret, C. Gervais, C. Brouder, N. Trcera, A. Bordage, I. Errea, and F. Mauri, Phys. Rev. B **92**, 144310 (2015).

[92] C. P. Schwartz, F. Ponce, S. Friedrich, S. P. Cramer, J. Vinson, and D. Prendergast, J. Electron. Spectrosc. Relat. Phenom. **218**, 30 (2017).

[93] M. Abramowitz and I. A. Stegun, *Handbook of Mathematical Functions with Formulas, Graphs, and Mathematical Tables* (Dover, New York, 1972).